Channelling optics for high quality imaging of sensory hair

C. Skupsch, T. Klotz, H. Chaves, and C. Brücker

Additional information on Rev. Sci. Instrum.

Channelling optics for high quality imaging of sensory hair

C. Skupsch,[a] T. Klotz, H. Chaves, and C. Brücker
Institute of Mechanics and Fluid Dynamics, TU Bergakademie Freiberg, Germany

A long distance microscope (LDM) is extended by a lens and aperture array. This newly formed channelling LDM is superior in high quality, high-speed imaging of large field of views (FOV). It allows imaging the same FOV like a conventional LDM, but at improved magnification. The optical design is evaluated by calculations with the ray tracing code ZEMAX. High-speed imaging of a 2×2 mm^2 FOV is realized at 3.000 frames per second and 1 μm per pixel image resolution. In combination with flow sensitive hair the optics forms a wall shear stress sensor. The optics images the direct vicinity of twenty-one flow sensitive hair distributed in a quadratic array. The hair consists of identical micro-pillars that are 20 μm in diameter, 390 μm in length and made from polydimethylsiloxane (PDMS). Sensor validation is conducted in the transition region of a wall jet in air. The wall shear stress is calculated from optically measured micro-pillar tip deflections. 2D wall shear stress distributions are obtained with currently highest spatiotemporal resolution. The footprint of coherent vortical structures far away from the wall is recovered in the Fourier spectrum of wall shear stress fluctuations. High energetic patterns of 2D wall shear stress distributions are identified by proper orthogonal decomposition (POD). © *2012 American Institute of Physics*. [http://dx.doi.org/10.1063/1.3697997]

I. INTRODUCTION

Imaging at high magnification is instrumental in many research disciplines. Important fields are femtochemistry, biology, solid mechanics and fluid mechanics. In this paper, the technical emphasis is on imaging of regular arrays of micro-sized objects in fluid mechanics with high-speed cameras. High-speed imaging requires high magnification because of larger pixel size, relative to standard CCD sensors. High-speed cameras exhibit a typical pixel size of some 10 microns.[1] For physical reasons, the chip size increases with increasing temporal resolution. Thus, for time-resolved microscopic imaging applications the pixel size is typically much larger than interesting object structure length scales. Consequently, the pixel size is the limiting quantity. In order to avoid this limitation the optical magnification should equal the ratio of pixel size and required spatial resolution. High-speed CCD and CMOS cameras are standard tools for flow *visualization*. For example, Wong *et al.*[2] carried out high-speed schlieren imaging at 1.000 frames per second (fps). Brian[3] presented 3D visualization of turbulent boundary layers with 500.000 fps. Thoroddsen *et al.*[4] observed the dynamics of the bubble pinch-off up at frame rates of up to 1 million fps. Recently, Skupsch *et al.*[5] have presented a digital high-speed Cranz-Schardin camera running at 40 million fps. Furthermore, high-speed cameras are used for *topological flow measurements*. For instance, the two-dimensional distribution of wall shear stress fluctuations is measured by arrays of wall-attached flexible sensory hair, called micro-pillars, at high spatial resolution (Brücker,[6,7] Grosse[8]). Micro-pillars are flow-sensitive hair with typical diameters of 30 μm or less. The magnitude and orientation of the fluid-imposed deflection is a measure of the two-dimensional wall shear stress. As the micro-pillar deflection is detected optically, the measurement uncertainty of the sensor is mainly affected by imaging quality. This motivates effort in developing specialized, high-quality optics.

In this paper, the micro-pillars are combined with a specialized optics forming a sensor that is superior for detecting the wall shear stress at high spatiotemporal resolution. The specialized optics consists of a long distance microscope (LDM), a lens and an aperture array. This channelling LDM allows imaging micro-pillars distributed on 2×2 mm^2 at an improved magnification of factor 17 and 3.000 frames per second. Up to now, there are no publications on experiments with micro-pillar fields observed at higher spatiotemporal resolution. Each micro-pillar is imaged through its own optical channel. Otherwise, the whole micro-pillar field would not fit onto the CCD-chip at present magnification. The micro-pillars used in this work are 20 μm in diameter, 390 μm in length and made from polydimethylsiloxane (PDMS).

In order to validate correct functionality, the pillar-sensor is applied to a wall jet. The working medium is air. The wall jet is generated by a nozzle connected to a plane wall (Figure 8). Following the definition by Launder and Rodi,[10] a wall jet can be regarded as a shear flow directed along a wall. Above the wall, the velocity in the shear layer exceeds that in the free stream. A lot of experimental work regarding the wall jet was published in last decades. Bajura[11] conducted velocity measurements by means of the hot-wire technique in a laminar plane wall jet. Eriksson[12] investigated the initial development of the turbulent plane wall jet by means of Laser Doppler velocimetry. Both found good agreement between experimental results and theory. Dejoan[13] presented a large eddy simulation basing on the results of Eriksson[12] consistent with the experiment. In the present work the wall jet is characterized by smoke visualization and particle image velocimetry (PIV).

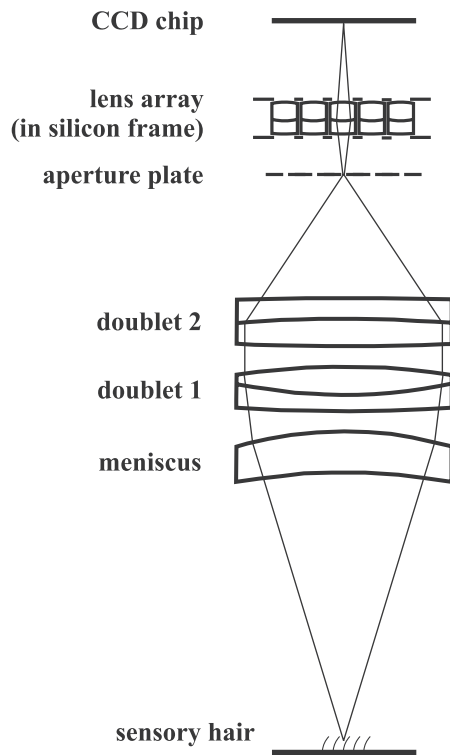a)Electronic mail: christoph.skupsch@imfd.tu-freiberg.de.

FIG. 1. Optics of the channelling LDM (height not to scale).

FIG. 2. Lens array and aperture plate.

As in former work regarding the transitional wall jet (Hsiau[14]) the jet Reynolds number and the axial measurement position is varied. Reynolds numbers range from Re = 1090 to Re = 2360, the axial section for PIV is $0 < x/d < 5$.

After validating the pillar-sensor, first results for wall shear stress patterns are obtained in the transitional region of the wall jet. The most common method for obtaining wall shear stress or skin friction is calculation from velocity data. For the fully developed turbulent wall jet the mean streamwise wall shear stress is deduced from the outer velocity profile, see Glauert.[15] For instance, Kunze[16] used the Glauert similarity solution for calibrating his wall shear stress sensor. In the transition region of the wall jet, it is more challenging to obtain the wall shear stress from velocity data. Eriksson[12] and Tachie[17] measured the velocity gradient at the wall in order to deduce the wall shear stress. Both worked at huge flow facilities several meters in length that reduced the resolution requirements for the used sensors. However, for table-top facilities conventional measurement techniques may lack in spatiotemporal resolution near walls, because of Fresnel and diffuse reflection of the used illumination, low density of tracer particles due to Saffman forces, to mention a few. Using micro-pillars attached to the wall can be the remedy. In the present wall jet distributions of wall shear stress fluctuations are investigated at $1 < x/d < 1.2$. The sensor provides simultaneously frequency spectra of vortical structures and the corresponding footprints in the wall shear stress fluctuation. The sensor setup including the optics in detail is described in Sec. II. Experiments are presented in Sec. III. Results are shown and discussed in Sec. IV, followed by conclusions in Sec. V.
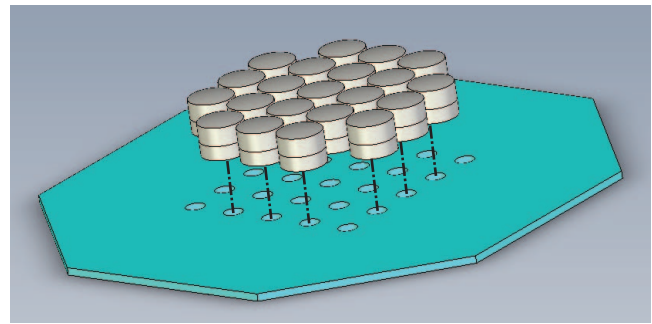
II. SENSOR SETUP

A. Optics

The optics in Figure 1 channels periodically aligned sections of the object via an aperture and a lens array. An LDM with $NA = 0.16$ numerical aperture provides 2.5 μm optical resolution within 2.15 mm field of view (FOV) diameter of the objective. It consists of three off-the-self lenses (meniscus, doublet 1, doublet 2) manufactured by CVI Melles Griot, USA. The lenses are built in retaining plates that are installed in a Microbench system by LINOS, Germany.

Twenty-one small doublet lenses purchased from Edmund Optics, Germany are aligned in an array, Figure 2. The aperture plate in Figure 2 exhibits concentric apertures, $D = 0.94$ mm in diameter. The apertures are aligned on-axis to the corresponding doublet indicated by straight lines. The lenses are clamped between two perforated mounting plates forming a frame. Lenses and plates are glued by poly-dimethylsiloxane (PDMS). The aperture and mounting plates are cut and etched silicon wafers purchased from GeSiM, Germany.

The LDM fits into a 35 mm diameter mounting tube. The working distance is 84 mm, measured from the edge of the meniscus. The LDM magnification is $m_{obj} = 6.25$, the array magnification is $m_a = 2.75$. The overall length from object to image is 740 mm. Lens parameters are listed in Table I.

1. Working principle

The idea of decomposing the FOV in single sections for high-resolution flow measurements of distributed regions of interest (ROI) was introduced by Bauer *et al.*[18] in 2009. In Figure 3, the working principle is sketched exemplarily for a text block as object. There are four ROI marked by circles. Let us assume only the four ROI are imaged simultaneously. In conventional imaging not only the circle diameter U of the ROI, but also the pitch p_o is magnified. Consequently,

TABLE I. Lenses of the channelling LDM.

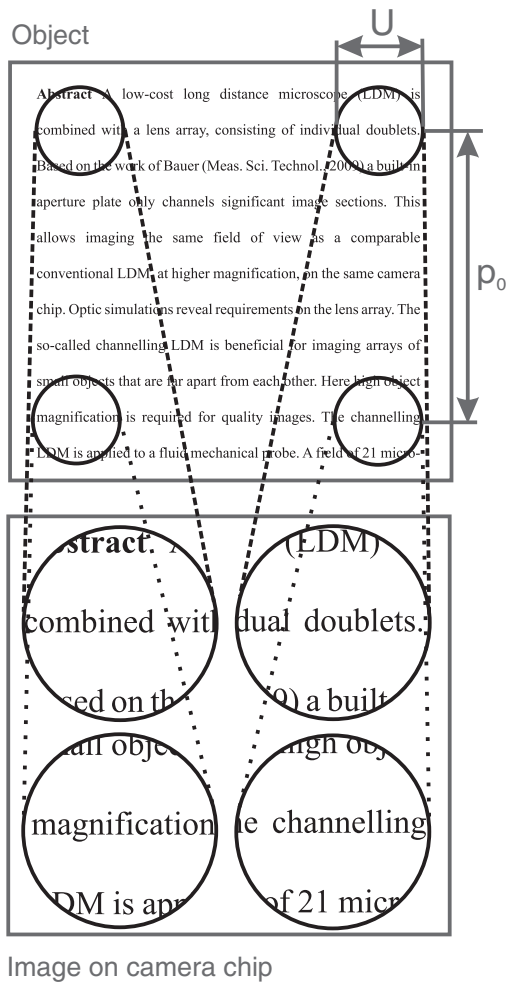|	Meniscus	Doublet 1	Doublet 2	Array lens
Focal length [mm]	233	160	600	9
Diameter [mm]	31.5	31.5	31.5	3

Object

U

p_0

Image on camera chip

FIG. 3. Channelling LDM applied to a text block (object), showing magnified regions of interest (image on camera chip).

the whole text block fills the whole format of the camera chip.

Alternatively, one may wish to select the ROI exclusively and image them at high magnification. The proposed method of an LDM combined with a lens array can provide decomposition and recombination of the text block as shown in Figure 3. The optical path in Figure 1 is as follows: the front objective (the LDM) images the whole text block on an aperture plate, magnified by factor m_{obj}. There, an intermediate image is generated. The aperture plate transmits the ROI, which are magnified additionally by the lens array at factor m_a. This leads to factor $m_{obj}m_a$ magnification of the ROI. Variation of m_a does not change the image of pitch p_o that is fixed by the LDM. The resulting image on the camera chip is shown in Figure 3. The quotient of the magnifications of U and p_o is the reduction factor r. It equals the array magnification $r = m_a$. In comparison to standard LDMs, at same magnification the channelling LDM allows to use a factor r^2 smaller chip area to image the ROI in Figure 3. Referring to Bauer[18] there is an upper limit for m_a that prevents overlapping of the channel images on the camera chip. With lens array pitch p_a and aperture window diameter D the maximal reduction

factor reads

$$r^{max} = p_a/D. \tag{1}$$

It is $r^{max} = 3.33$, determined by the geometry of lens and aperture array ($p_a = 3.13$ mm, $D = Um_{obj} = 0.94$ mm). Another useful parameter is the in-line ROI filling factor $\sigma = Um_a m_{obj}/p_a$. Substituting $m_{obj} = p_a/p_o$ yields Eq. (2). Maximal chip filling equals $\sigma = 1$,

$$\sigma = Um_a/p_o. \tag{2}$$

The number of ROI that can be imaged in-line on the camera chip is $n = l/p_a$, with l the camera chip size. In the present setup the parameters are as follows: $U = 150$ μm, $n = 5$ and $\sigma = 0.82$.

2. Building a simple LDM

Commercial LDMs usually contain expensive lens configurations, causing strong push to develop optics basing on cheap components. Douillet *et al.*[19] propose a simple high-resolution imaging lens system. It consists of a specially designed meniscus shaped lens (short: meniscus) followed by two doublets. This lens configuration has been adapted in this work. The major correction of the LDM regards lower-order spherical aberration. The correction does not affect off-axis aberrations like coma, astigmatism and field curvature, because of axial asymmetry of the LDM.[20] A meniscus is the appropriate front lens to minimize primary spherical aberration W_{040} at high object apertures. A mathematical description of W_{040} is found in Geary,[21]

$$W_{040} \propto \left(u - \frac{y}{R} \right)^2. \tag{3}$$

Equation (3) is valid for one lens surface. W_{040} is a function of the angles u (incident ray) and y/R (surface normal). The parameter y denotes the position on the pupil and R the radius of surface curvature. A ray originating at distance w to the meniscus with an angle u to the horizontal is illustrated in Figure 4.

Spherical aberration W_{040} diminishes for rays that are parallel to the lens surface normal. The same argument is valid for the second lens surface. In order to retain refractive power, forward and backward surface curvatures have to be slightly different.

Accounting the lens maker's formula,[22] a well-corrected meniscus has a focal length larger than R. As the working distance w should equal R, a stand-alone meniscus never forms real images. Doublet 1 in Figure 2 reduces the original focal length of the meniscus. The focal length of doublet 1 can be

surface normal
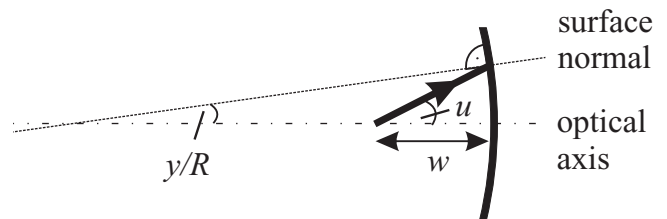
optical axis

y/R

y u

w

FIG. 4. Ray hitting meniscus non-parallel to surface normal.

calculated by thin lens approximation for imaging to infinity. The image is formed by doublet 2 defining the total magnification of the LDM.

3. Lens array

The simplest lens array is composed by regularly arranged, identical spheres. The optical axis of each sphere points a different object position, leading to two characteristic imaging properties. Firstly, off-axis aberrations over the array can be reduced.[23] Consequently, a lens array can image extended objects at better spatial resolution than a single sphere with same focal length. Secondly, each array lens channels a well-defined part of the object.[24] The latter property is more elementary for this paper, as the spatial resolution is limited by the LDM and not by the lens array.

The lens array is made of commercial doublets, arranged with 3.13 mm pitch, see Figure 5. The four corner lenses are left out for practical reasons. Altogether, there are 21 optical channels.

The channels are divided into five groups, indicated by index i of the radius r_i, Figure 5. For each of the five groups, the optical transfer function is calculated. Its modulus, the modulation transfer function (MTF), is chosen as the criterion for image quality. Undisturbed object contrast corresponds to the maximum MTF = 100%. However, in practice, lenses will attenuate object contrast. The contrast of an object imaged through the channelling LDM equals the MTF.[21] As the LDM is poorly corrected against off-axis aberrations, imaging quality deteriorates for increasing group index i. At present conditions with an optical magnification M = 17, the spatial resolution calculates to 2.5 μm or in other words 23 lines/mm spatial frequency in the image. The resulting MTF is larger than 10% for each channel at this frequency confirming the desired imaging performance.

Further, the benefit obtained by doublets in the lens array is quantified. The radius of wave-front curvature increases in propagation direction. Therefore, the imaging quality of the lens must depend on the ratio of image and object distance. An optical ray-tracing simulation with ZEMAX considers this dependency. A doublet is compared to a typical equi-convex lens with identical focal length. The analysis is carried out on-axis for the intermediate image aperture $NA_{int} = 0.03$,

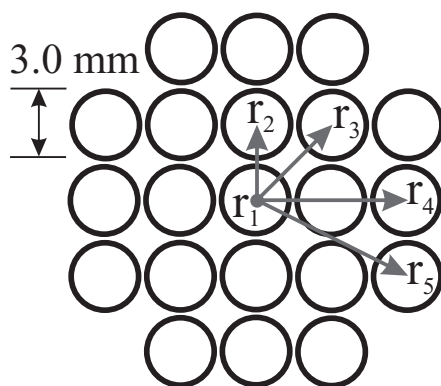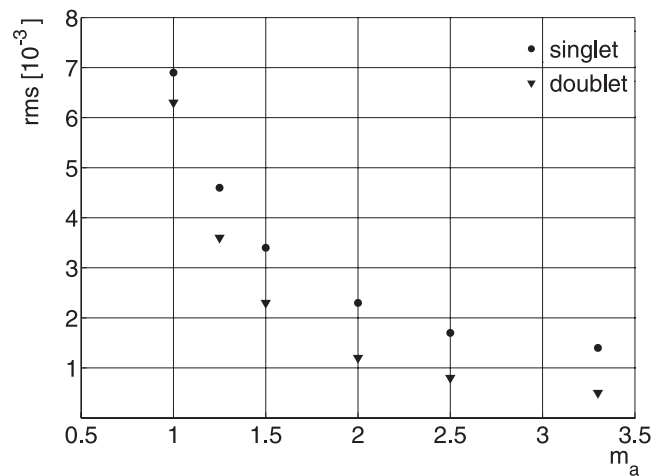FIG. 6. Comparison of rms aberration of singlet and doublet lens at different magnification.

corresponding to the present setup and for the wavelength $\lambda = 532$ nm.

In Figure 6, the simulated wave-front standard deviation *rms* (wave-front aberration) is plotted in waves as a function of magnification m_a. Large m_a means large reduction r of the channelling LDM. Aberration decreases with increasing magnification for both singlet and doublet. As expected, a doublet array allows imaging at considerably higher quality. In experiments $m_a = 2.75$ is realized.

B. Micro-pillars

The micro-pillars used in this work are displayed in Figure 7. They are made from polydimethylsiloxane (PDMS), $L = 390$ μm long and $d = 20$ μm in diameter. The PDMS forming the micro-pillars is free from air pockets. A two-dimensional array consisting of 30 × 30 micro-pillars is used for experiments. The micro-pillars are spaced equally by 500 μm in a quadratic array. The array is microfabricated in our laboratory by a specially developed etching process. A silicon mask is used as mold for casting the micro-structures, as presented by Kim.[25]
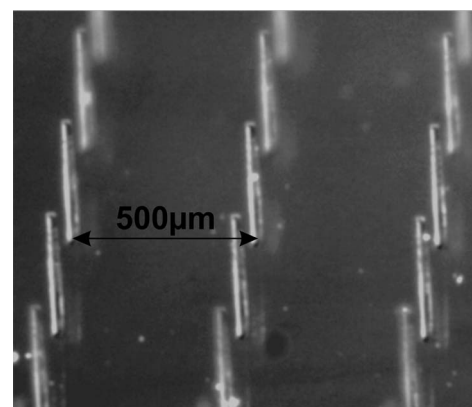

FIG. 7. Subsection of the 30 × 30 micro-pillar field as seen by a standard microscope. The image demonstrates good quality and homogeneity of the cylindrical structures.

FIG. 5. Lens array geometry.

III. EXPERIMENT

A self-made nozzle generates the wall jet in still air, Figure 8. The nozzle is similar to that used by Kunze *et al.*[16] It has a rectangular cross section $L = 120$ mm in length and $d = 5$ mm in height. The aspect ratio at the nozzle exit is $L/d = 24$. The nozzle is connected to a pressure vessel. The flow is driven by a constant pressure head with a valve. In order to learn about the jet formation at certain pressure values, top views of the flow onto the wall are visualized using nebulizer fluid. Later, particle image velocimetry (PIV) is applied to determine accurate jet Reynolds numbers and present coherent flow structures. Referring to Eriksson,[12] the flow Reynolds number is a function of half the nozzle height d and the mean, maximum axial velocity u_m at the axial position of interest,

$$\mathrm{Re} = \frac{u_m d/2}{\nu_{air}}. \tag{4}$$

After the visualization study, the micro-pillar sensor is applied to the wall jet. The measurement quantity is the wall-parallel tip displacement of the micro-pillars and the bending direction under fluid-imposed load. The bending is determined relatively to the location of the tip for zero flow conditions at rest. It can be related to the viscous forces acting on the cylindrical structure of the micro-pillar and therefore to the local wall shear stress components. The measurement uncertainty of the sensor depends mainly on the achievable optical resolution[9] motivating the efforts in developing specialized optics. An image resolution of 1 μm per pixel and an optical resolution of 2.5 μm over the complete field of view (FOV) are feasible by the developed optics. High temporal resolution is obtained by a Photron FASTCAM APX-RS 1024×1024 px high-speed camera equipped with the LDM. It records the motion of micro-pillar heads at 3.000 fps. The flow visualization is presented in Sec. III A. Section III B is about the static and Sec. III C about the dynamic sensor calibration, followed by the wall shear stress measurement in Sec. III D.

A. Wall-jet visualization

Typical flow structures developing in the transitional wall jet are documented by classical flow visualization pictures.
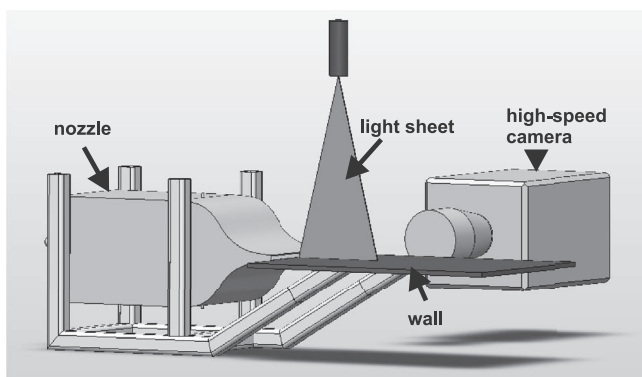
FIG. 8. Wall jet generator and flow visualization system. The light sheet and camera position is shown in orientation for the PIV-measurements.

Smoke is injected into the settling chamber upstream of the nozzle and the jet flow is illuminated downstream by a standard halogen lamp. Images are taken with a Photron FAST-CAM APX-RS camera with its optical axis aligned normal to the wall. Recordings are shown in Figure 9. The flow direction is from left to right. The images show 30×50 mm^2 of the x-z plane. The exit of the nozzle is at x = 0. Smoke images reveal the regular appearance of spanwise large rolled-up structures, short: roller, downstream of the nozzle exit. These rollers are formed by the shear layer roll-up. They develop spanwise instabilities as indicated by the spanwise waviness. At the leading edge of these waves, streamwise secondary flow structures are detected as bright horizontal stripes. One aim of this work is to investigate the developing process of theses stripes. Therefore, their point of generation needs to be shifted near the micro-pillar array by varying the Reynolds
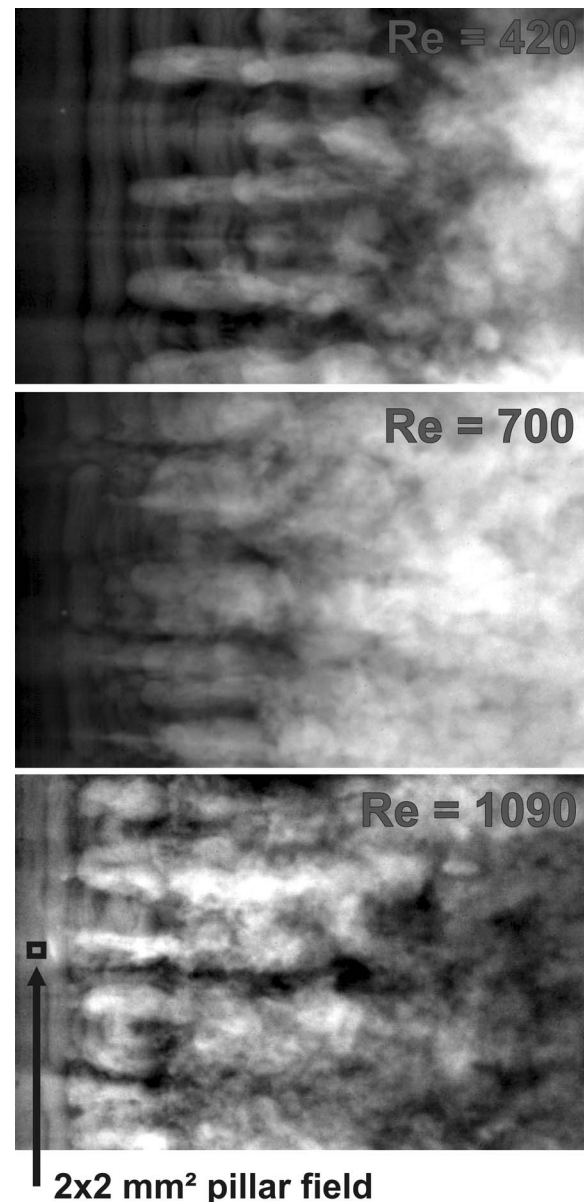
FIG. 9. Smoke visualization of the wall jet. View from top onto the wall. The location of observed micro-pillars is indicated by a square in the bottommost image.

number, see Figure 9. For increasing Reynolds number the transitional region shifts closer to the nozzle exit. Turbulent conditions are reached earlier in the jet history. This is caused by increasing instability in the outer layer.[14] The observed streamwise oriented secondary structures forming on the jet are similar to the secondary vortex structures generated in the wake of a cylinder examined by Williamson *et al.*[26] The extension of the imaged micro-pillar field is smaller than half a streamwise period of the visualized rollers, note the square in Figure 9. Later, this is important for accurate frequency detection of the roller without spatial averaging.

Dejoan[13] states the maximum mean velocity u_m in equation (4) is approximately constant within the range of $0 \leq x/d \leq 5$. The 2×2 mm^2 micro-pillar array is located in the section $1 < x/d < 1.2$. Consequently, the jet Reynolds number is constant above the array. The velocity u_m is extracted from 2D velocity fields as displayed in Figure 10, determined by particle image velocimetry (PIV). The velocity fields are determined within the light sheet from Figure 8. A Pegasus laser by New Wave Research, USA, with 6 mm beam diameter and 10 mJ peak power is reshaped to a sheet of 500 μm thickness by self-designed light sheet optics. The nebulizer fluid Blitz Reflex by SAFEX, Germany, is used as tracer. It is injected in the nozzle flow via bypass. 2048 images are recorded at 2500 fps with a FASTCAM APX-RS by Photron, USA. The interframe time of double images is 50 to 200 μs. The ensemble average of the velocity fields at Reynolds number Re = 1290 is shown in Figure 10. The velocity profiles are similar to those shown in Eriksson *et al.*[12] for a transitional wall jet. Smoke visualization and PIV measurements confirm the presence of transition at the micro-pillar field location.

The near-wall region of the transitional wall jet is analyzed for six different Reynolds numbers. At $1 < x/d < 1.2$ the corresponding maximal velocities u_m range from 6.7 m/s (Re = 1090) to 14.5 m/s (Re = 2360).

In Figure 11 one period of the roll-up process of a large vortical structure is presented for Re = 1290. The snapshots are spaced equally in time. Within 1.6 ms, one period passes through. This equals the roller frequency $f_{roller} = 625 \pm 50$ Hz. The uncertainty results from 200 μs discrete interframe time.

The large vortex in Figure 11 is a primary vortex generated by Kelvin-Helmholtz instabilities.[14] As these structures interact with the wall, pairs of counter-rotating secondary vortices are generated, which are oriented in streamwise direction. Primary vortices induce streamwise

FIG. 11. Image sequence showing one period of the quasi-periodic roll-up of larger vortical structures. The dashed line indicates the reference location, where the first picture of the sequence shows the same position of the roller structure as the last one. The five vertical, white bars in the uppermost image indicate the position of the micro-pillars. Each bar corresponds to one micro-pillar. The height of the bars is enlarged about four times, whereas their lateral distance scales correctly.

fluctuations, whereas secondary vortices induce spanwise ones.

B. Static sensor calibration

The calibration of the sensor consists of two steps. In step one, the static deflection of the micro-pillars is determined at constant load in a calibration facility. In step two, the frequency response, of the micro-pillars is measured, which is needed for dynamic measurements.

Calibration step one is performed in a self-made planar Couette flow facility. A conveyor belt mounted in transparent mineral oil generates a flow with linear velocity profile. An electrical motor drives the conveyor. The micro-pillar field is mounted in such way that the base is flush with the channel
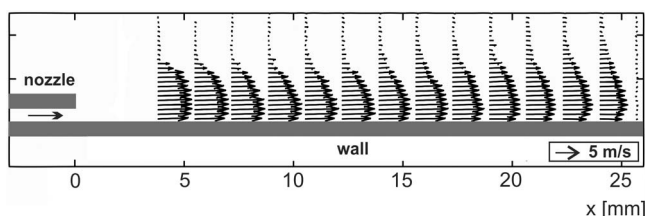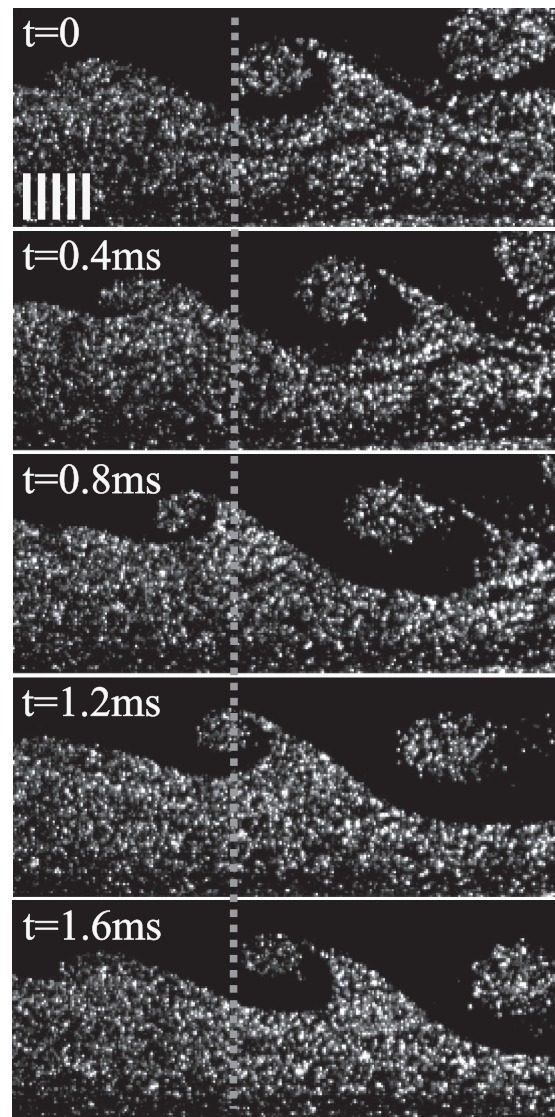

FIG. 10. Ensemble average of the cross-sectional velocity field downstream of the nozzle, measured by classical PIV. The jet Reynolds number is 1290. The profiles show the development of the wall jet in the transitional region.

wall and the micro-pillar tips protrude into the flow. Micro-pillar tips are imaged onto a mvBlueFOX 224G CCD camera by Matrix Vision, Germany, with 0.5 μm/px image resolution. The wall shear stress τ in a plane laminar Couette flow with a fixed wall and the opposite belt wall in streamwise motion varies linearly with velocity U of the belt, e.g., Schlichting,[27]

$$\tau = \rho \nu \frac{U}{h}. \tag{5}$$

The load on the micro-pillars is varied by changing the belt velocity. The working fluid is Shell Ondina 913 mineral oil. Following Shell data the density is $\rho = 839 \ kg/m^3$. The kinematic viscosity is determined by an Ubbelhode viscometer made by Schott. It is $\nu = (14.33 \pm 0.07) \ mm^2/s$ at a temperature of 21.2 °C. The channel gap between belt and opposite fixed wall was set constant to $h = 6.3$ mm. The belt velocity is varied in the range $0.1 \leq U \leq 0.6$ m/s.

At given wall shear stress an edge-finding algorithm is used to determine the displacements of micro-pillar tips relative to their location at rest. Displacements are averaged over 1000 recordings. Four micro-pillars are imaged simultaneously for analysis. The systematic uncertainty is 0.5 μm. Deflections w scaled by the micro-pillar length L are given in Figure 12. Correct operation of the calibration facility is checked by side views of the micro-pillars. The side view reveals the oil penetrates completely the space between the micro-pillars. There are no air pockets. Further, the bending is proved linear elastic.

For characterization of the flow around the micro-pillar, another Reynolds number formed by the micro-pillar diameter and the tip velocity needs to be introduced. Although, the Reynolds numbers for the Couette flow and the wall jet are different, the micro-pillar Reynolds number is similar in both flows, as confirmed by PIV measurements.

The micro-pillar deflection does not increase proportionally with increasing shear stress, Figure 12. This deviates from the expected linear trend as derived theoretically by Brücker.[6] There are two conditions, which are supposed to

FIG. 13. Visualization of the flow structure in the wake of a wall-bounded cylinder with a free end at pillar Reynolds number Re = 33. The flow is from left to right. The illuminated plane is centered with the incoming flow direction and the pillar axis.

be causing this deviation. Firstly, the theoretical drag coefficient from the Oseen-approximation is only valid for an infinite cylinder.[28] Secondly, more critical are the wall effect and the free-end overflow, which affect the drag force distribution on the micro-pillar structure. Exemplarily, Figure 13 shows the contribution of both effects on the flow around a pillar structure by means of a flow visualization picture. The Reynolds number of the displayed pillar is Re = 33.

In the immediate wake of the micro-pillar, there is a strong wall-normal flow away from the wall towards the tip of the micro-pillar. This cross-flow meets with a second counter-acting cross-flow, which results from the flow over the free end. Therefore, the drag forces per unit-length along the cylinder are supposed to vary in a more complex way than a simple linear trend. Both effects need to be considered for correct modelling of the micro-pillar bending. The calibration curves take into account this non-linearity. The derived exponential curve fit is only valid for small bending conditions with $w/L < 0.1$. Structural excitations of the micro-pillars can be excluded in the small bending range. Deflections $w/L < 0.05$ are realized in experiments.

C. Dynamic sensor calibration

Calibration step two, analyzing the dynamic response, is realized by oscillation experiments in air. Brücker *et al.*[9] report comprehensively on the theory of the dynamic response of micro-pillars. They demonstrate the micro-pillar sensitivity increases significantly for flow frequencies near the natural frequency f_0 because of non-linear ringing. They state linear response within the range $0 \leq f/f_0 \leq 0.3$. Flows with frequencies beyond that range could lead to erroneous dynamic wall shear stress data. It might be noted, the oscillating nature of micro-pillars in air is barely investigated so far. In air the range of linear response is larger than in liquids, due to the larger natural frequency. Especially, the rate of stored
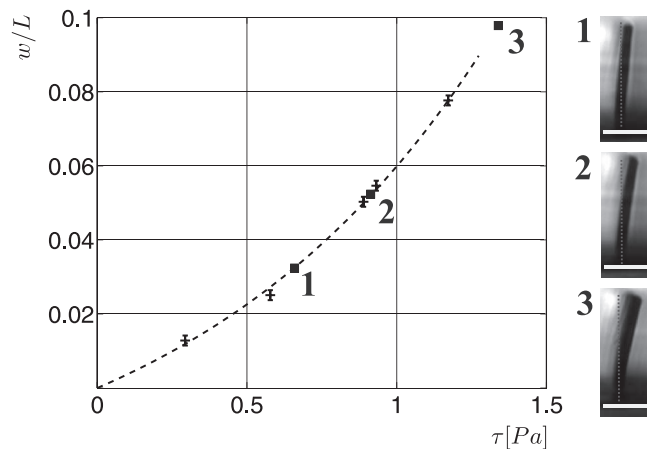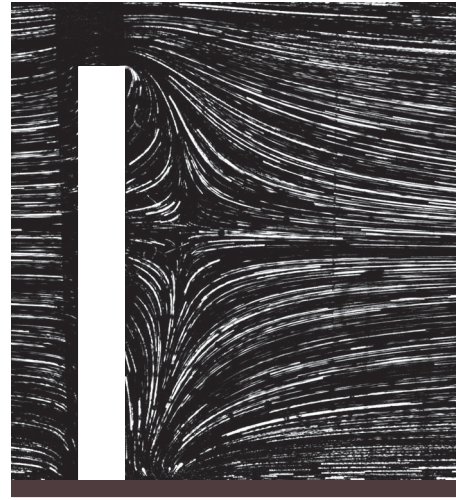

FIG. 12. Calibration curve showing the normalized micro-pillar-tip deflection at different wall shear stress in the lower limit of load range. Calibration is carried out in a Couette flow apparatus generating a constant velocity gradient within the flow channel. +calibration data; ■micro-pillar side view; –fit of calibration data to equation $w/[\mu m] = \exp(\tau/[Pa] + 2.6099) - 13.597$.

energy relative to energy dissipation by oscillation (Q-factor) grows by factor 50 in air compared to water.

The natural frequency of an oscillating micro-pillar is determined experimentally. One micro-pillar is cut out of a complete array and fixed on a carrier. It is positioned in air in front of a light source and imaged onto the Photron APX-RS high-speed camera at 34.000 fps. The micro-pillar is excited by a metal cantilever mounted on a micropositioning unit by LINOS, Germany. The time signal of the damped oscillation is analyzed. The natural frequency of the micro-pillars in air is $f_0 = (2.8 \pm 0.05)$ kHz.

In a next step the sensitivity of the micro-pillar field is determined for the frequency spectrum 200 Hz $\leq f$ $\leq$ 3.000 Hz. Therefore, the complete field is positioned in a realistic, oscillating air flow. The flow is generated by two high quality speakers by Beyma, Spain. The speakers are aligned face to face at 40 mm distance to each other. They are driven by 80 W electrical power generated by an amplifier and a function generator providing sine waves. The micro-pillar motion is recorded by the Photron camera at 10.000 fps. Due to automatic frame size reduction each image is 384 × 560 px corresponding to a number of six simultaneously observed micro-pillars. The optics is the same as described in Sec. II. Optics and speakers are vibration-decoupled. The setup is sketched in Figure 14.

The speakers are characterized by a laser Doppler vibrometer (Polytec, Germany). As the maximum cone excursion decreases with increasing frequency, the maximum particle velocity in the oscillating flow decreases as well. In order to measure that decrease the maximum velocity of the speaker cone v_{max} is determined as a function of the speaker frequency f, Figure 15. The velocity decreases exponentially with increasing frequency.

Following Brücker[9] the sensitivity of a micro-pillar is the maximum deflection amplitude scaled by the wall shear stress. As the wall shear stress is proportional to the velocity in the flow, the deflection can be scaled by the latter as well. The resulting sensitivity, the ratio of the maximum deflection amplitude of the micro-pillars and the maximum cone velocity w_{max}/v_{max}, is plotted in Figure 16. The maximum deflec-
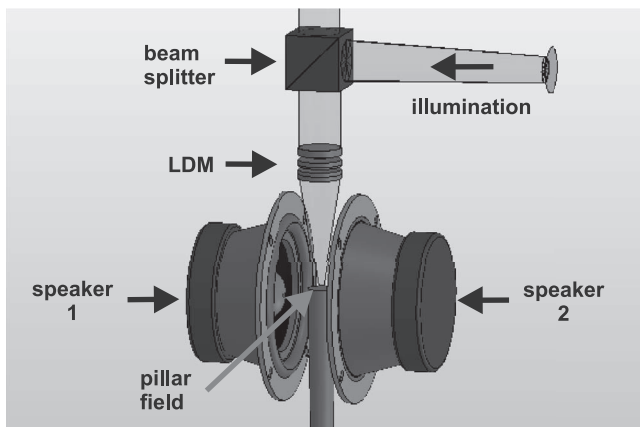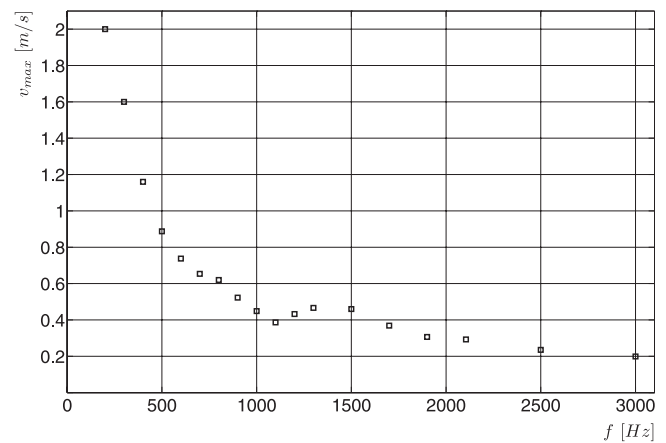

FIG. 15. Maximum velocity of the speaker cone as a function of the speaker frequency.

tion is determined by an edge finding algorithm in 10.000 images at six micro-pillars. Deflections range from 3.5 to 11 μm. A Fourier transform of the obtained data reveals exact matching of the frequency of the oscillating flow and the speaker frequency, which is forced by the function generator.

The sensitivity is constant for $f < 900$ Hz forming a plateau in Figure 16. Up to $f = 1300$ Hz it increases slightly by a factor of 1.6 relative to the plateau. Consequently, the micro-pillar field can be used for frequency measurements up to $f = 1300$ Hz. Without comprehensive knowledge of the sensitivity function the present micro-pillar field may not be used for frequency measurements at $f > 1500$ Hz, as Figure 16 indicates ringing for this range. Measuring frequencies $f > 1500$ Hz would require smaller and stiffer micro-pillar structures. According to Sec. III A, the most dominant periodic structure for the present wall jet is the natural roll-up of the spanwise vortices, compare Figure 11. The roller frequency is $f_{roller} = (625 \pm 50)$ Hz. As this is on the sensitivity plateau in Figure 16, we exclude significant contribution of non-linearity, like ringing, when

FIG. 14. Setup for dynamic calibration. The micro-pillar field is located directly between two speakers, observed by the channelling LDM.
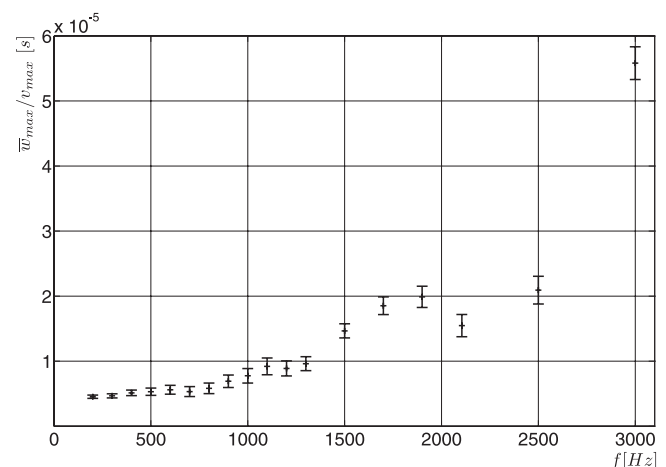

FIG. 16. Sensitivity of the micro-pillar field as a function of the frequency of the oscillating flow.
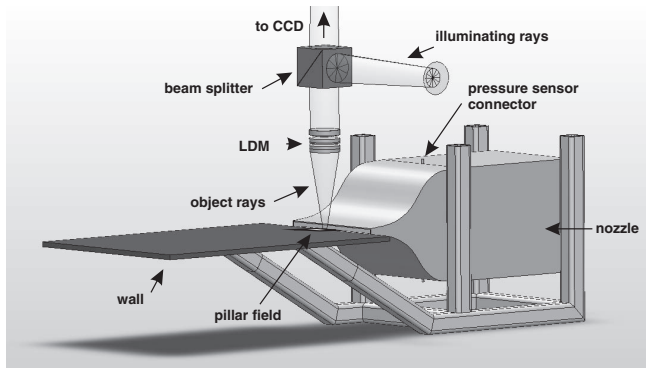
FIG. 17. Setup for wall shear stress measurements in a wall jet by means of channelling LDM.

detecting the roller dynamics with the present micro-pillar field.

D. Wall shear stress measurement

A subset of 5 × 5 micro-pillars is imaged with the channelling long distance microscope (LDM) at 2.5 μm optical resolution and M = 17 magnification. The optical axis of the LDM is aligned normal to the wall, see Figure 17. The used high-speed camera is a Photron FASTCAM APX-RS 1024 × 1024 px with 17.4 μm pixel size with 1 μm/px image resolution. The channelling LDM works in reflected-light mode. Illumination is realized by a self-designed Köhler illumination with a high-power LED light source. A beam splitter separates illumination and object rays. To enhance imaging quality an interference filter for 532 nm confines the spectrum of the LED. The optics, including the camera, is vibration-decoupled.

Imaging at high spatial resolution is realized by the high aperture of the LDM. The resulting shallow depth of focus leads to blurred images of the micro-pillar tips for large deflections, which are therefore analyzed by an edge-finding algorithm. The displacement of micro-pillar tips is resolved to ±0.5 μm. Micro-pillar deflections for small jet Reynolds numbers are analyzed by means of 2D cross-correlation in MATLAB. Only deflections smaller than one micro-pillar diameter ($w < 20$ μm) are considered for this analysis. Under practical conditions the sub-pixel accuracy for detecting the center of the tip is approximately 15% of the pixel size, leading to an uncertainty $\varepsilon_W = 0.15$ μm. This calculates to a resolution of the wall shear stress of 7 mPa.

Wall shear stress measurements are carried out in a wall jet at $1 < x/d < 1.2$. The laser Doppler vibrometer is used to measure vibrations of the wall (Figure 17), which might affect the micro-pillar motion. Detected vibration amplitudes are less than 0.2 μm at frequencies lower than 150 Hz. Therefore, external contribution to the micro-pillar oscillation is neglected. For each Reynolds number, 2048 images are recorded at 3.000 fps. Raw images are displayed in Figure 18. The upper image contains the micro-pillar field at rest. The lower one shows deflected micro-pillars at Re = 1650. Note the slight blurring of the deflected micro-pillar tips because of the shallow depth of focus of the LDM.

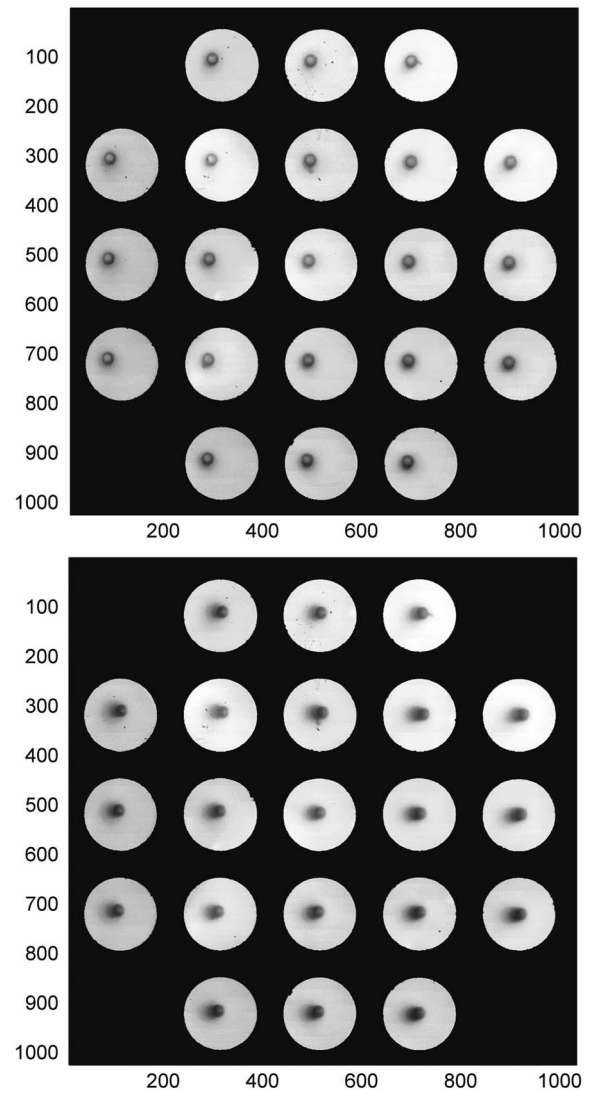FIG. 18. Images of the micro-pillar array at rest (top) and with arbitrary deflection at Re = 1650 (bottom). The flow direction is from left to right.

IV. RESULTS AND DISCUSSION

A. Sensor validation

The wall shear stress is calculated from measured deflections of the micro-pillar tips, Figure 18, and the calibration function given in Figure 12. Mean wall shear stress for different Reynolds numbers is shown in Figure 19(a). It is determined by means of temporal (2048 recordings) and spatial averaging (over the span of the micro-pillar array).

The mean local friction coefficient C_f is displayed in Figure 19(b). Experimental data is compared to theory. The dotted line is the theoretical wall shear stress for a turbulent wall jet given in equation (6).[27] It is deduced for a fully turbulent wall jet at the nozzle exit, without any laminar entrance flow,

$$\frac{2\bar{\tau}_u}{\rho U^2} = C_f = 0.0592 \left(\frac{Ux}{\nu}\right)^{-\frac{1}{5}}. \qquad (6)$$
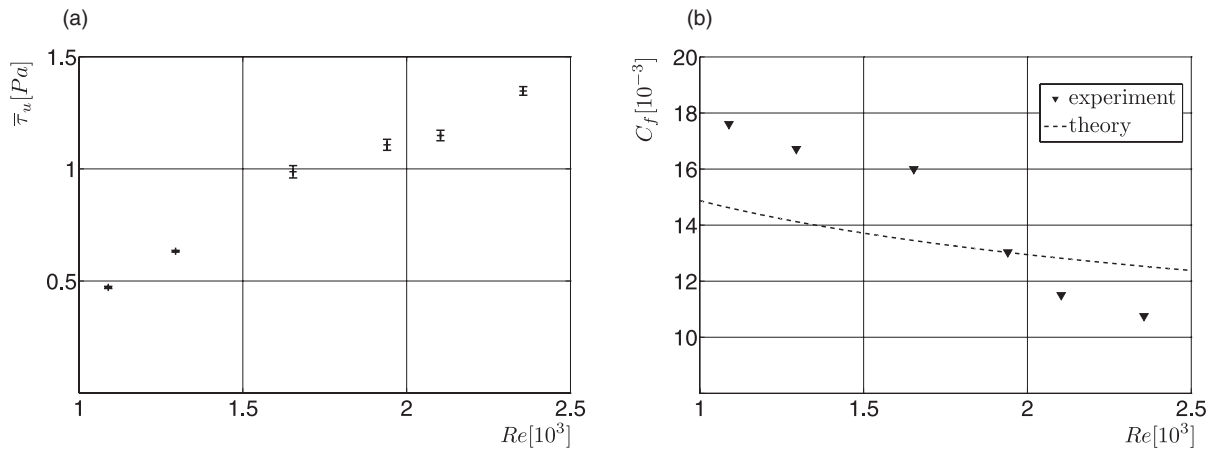
FIG. 19. (a) mean wall shear stress in streamwise direction $\bar{\tau}_u$, (b) mean friction coefficient C_f for different Reynolds number of wall jet. The location of the micro-pillar field is at $1 < x/d < 1.2$.

The observed deviation from theory is due to entrance flow effects and transition in the outer layer of the wall jet. When measuring in a transitional flow, it is worth having a look on the probability density function (PDF) of the wall shear stress fluctuations. The wall shear stress dynamic fluctuations may be analyzed, as there is no excitation of the micro-pillars due to flow conditions like non-linear ringing and no external vibration of the experimental apparatus. Fluctuations of the streamwise wall shear stress component reach up to 18% of the mean in the present experiment. In Figure 20, the PDF is shown for each Reynolds number in streamwise direction. Fluctuations in spanwise direction are left out, as their amplitude is much smaller. Yet, spanwise fluctuations must be regarded in the structural analysis.

At Re = 1090 the PDF exhibits almost laminar character. At Re = 1290 the PDF becomes asymmetric with regard to $\tau_u' = 0$ indicating the transitional nature of the flow. For clarity the PDF at $Re_m = 2360$ is plotted in Figure 21. The measured fluctuations are fitted by a skewed-normal distribution $PDF = 0.003 \cdot \exp[8.5(\tau_u'/[Pa]$
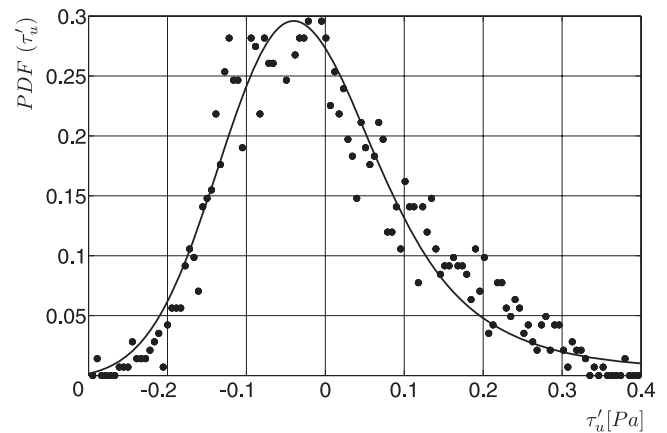

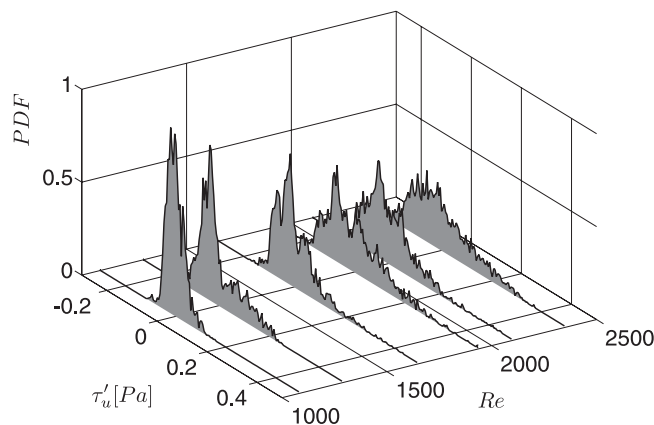FIG. 21. PDF of τ_u' at Re = 2360, fitted by a skewed Gaussian profile.

FIG. 20. Probability density functions (PDF) of streamwise wall shear stress fluctuations τ_u' for different Reynolds numbers of the wall jet. The location of the micro-pillar field is at $1 < x/d < 1.2$.
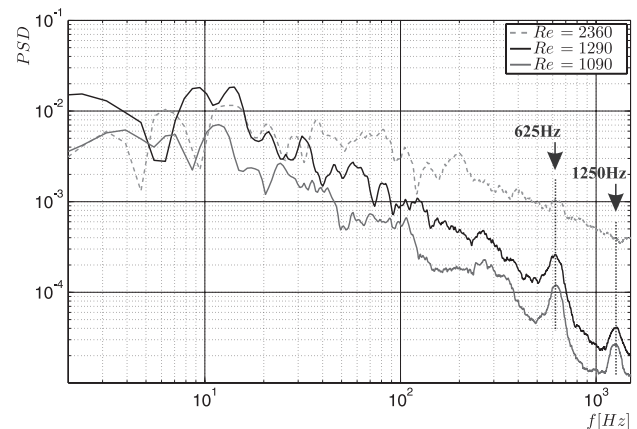

FIG. 22. Spectrum of wall shear stress fluctuations in the transitional wall jet at $1 < x/d < 1.2$. The frequency of the shear layer roll-up $f = 625$ Hz and its doubling are highlighted.
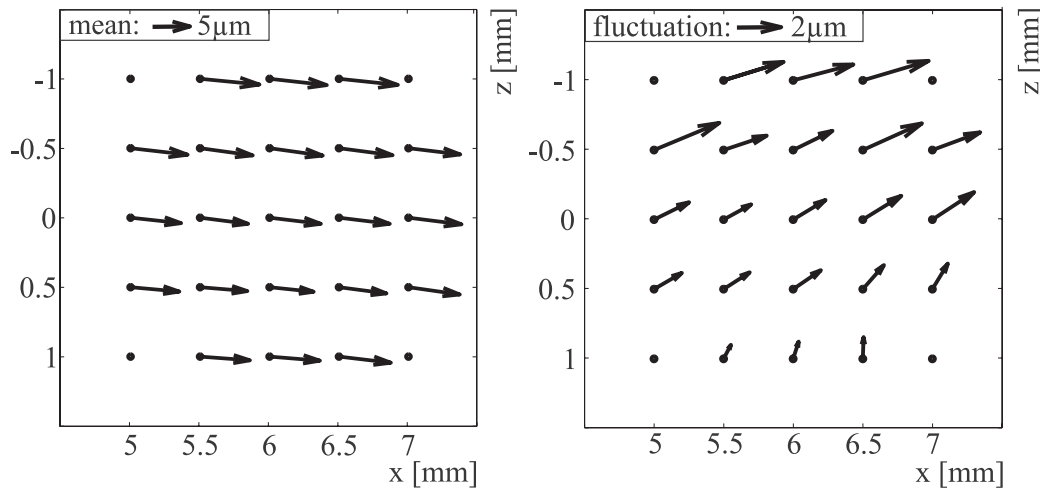
FIG. 23. Mean deflection and arbitrary snapshot fluctuation of micro-pillars in the transitional wall jet at Re = 1090 and 1 < x/d < 1.2. The direction of the flow is from left to right.

$- 0.712)^2] \cdot [1 + erf(7.97\tau_u'/[Pa])]$. Due to the roll-up of secondary vortices at the measurement position, the maximum of the skewed Gaussian is at $\tau_u' = -0.04$ Pa. The long positive tail of the PDF in Figure 21 indicates more frequent positive fluctuations than negative ones. Positively skewed PDFs are typical for turbulent shear layers as reported by Colella, for instance.[29]

B. Near-wall flow features

A spectral analysis is carried out for wall shear stress fluctuations at Re = [1090, 1290, 2360]. Sensing the micro-pillar motion is very sensitive at lower Reynolds numbers, as micro-pillar deflections are determined by cross-correlation here. The power spectral density (PSD) is presented in Figure 22. A Hanning window filter is applied to the quint-averaged spectra. The peak at $f = 625$ Hz clearly corresponds to the roll-up of the shear layer shown in the visualization study in Figure 11. The roll-up creates a footprint in the wall shear stress field. It corresponds to the quasi-periodic convective passage of the rollers in a plane further away from the wall in the shear layer. The second harmonic peak at $2f_{roller} \approx 1250$ Hz hints at the presence of vortex pairing in the formation of the larger rollers. Therefore, the large coherent structures are very likely generated by vortex pairing at the early stage of shear-layer roll-up. The discovery of structural events in the flow in the spectrum of wall shear stress fluctuations confirms correct dynamic response of the sensor. We conclude the dynamic wall shear stress fluctuations in the near-wall region for the most part reflect vortical structures in the high energetic fluctuation zone of the transitional flow.

The micro-pillar array is also used for topologic measurements in near-wall flows (compare Brücker,[7] Grosse[8]). An analysis of the topological characteristics of the near-wall flow structures and the corresponding wall shear stress distributions is presented for the lowest Reynolds number. The proper orthogonal decomposition (POD) technique is applied to micro-pillar deflections, see, e.g., the POD re-

view of Berkooz.[30] The mean deflection is subtracted from the snapshots leading to snapshot fluctuations, Figure 23. The magnitude of deflection is coded in the arrow length in the vector plot. Obviously, the mean vectors are not parallel to the streamwise flow direction. This is due to a non-perfect, slightly oblique mounting of the micro-pillar array relative to the main direction of the flow.

The fluctuation in Figure 23 can be composed of fundamental modes. These modes represent high energetic flow structures. They are determined by solving an eigenvalue problem in the POD. The eigenvalues correspond to the fraction of kinetic energy in the mode. The first three modes ϕ^1, ϕ^2, ϕ^3 contain 73.7%, 17.2% and 4.2% of the total kinetic energy. The time series of POD coefficients a_1, a_2, a_3 is given in Figure 24.

The fluctuation in Figure 23 is present in the time series at time step number 1884. It can be recombined for the most part by the first three modes and their amplitudes $\tau'(x, z) = a_1\phi^1 + a_2\phi^2 + a_3\phi^3$. The ratio of amplitudes for this fluctuation is $a_1: a_2: a_3 = 2.2: 1.2: 1$.

Consider the modes ϕ^1, ϕ^2, ϕ^3 depicted in Figure 25. Mode ϕ^1 is a contracting flow structure. It is formed either in the center of high-speed streaks (in positive direction) or in the center of low-speed streaks (in negative direction) both
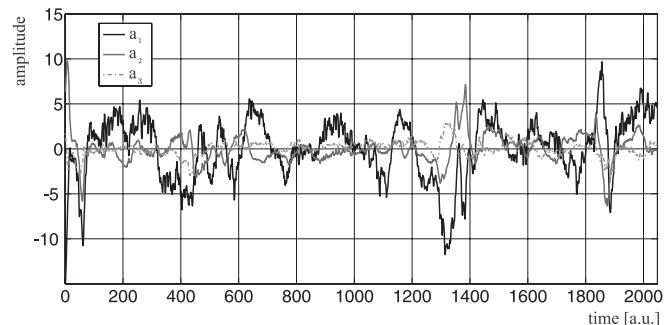

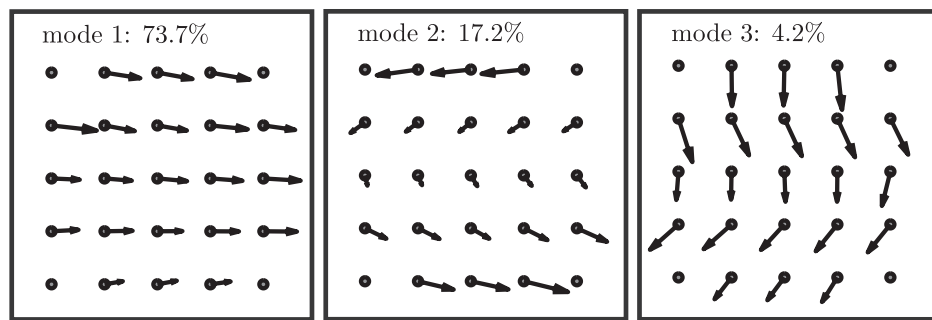FIG. 24. Time series of the first three POD coefficients at Re = 1090 and 1 < x/d < 1.2.

FIG. 25. High energetic POD modes ϕ^1, ϕ^2, ϕ^3 of wall shear stress fluctuations obtained by measuring the fluid-imposed deflections of twenty-one micropillars at Re = 1090 and $1 < x/d < 1.2$. The direction of the flow is from left to right. The contribution to the total energy is given in percent above the vector field.

directed streamwise. These streaks could be the initial disturbances of the roll-up process, which may lead to the formation of the secondary vortex structures shown in Figure 9. With factor 0.74 contribution to the total energy, it is the most dominant structure. Mode ϕ^2 is a shear structure formed by downstream and upstream fluctuations with comparable strength. It is only present near the edges of the high-speed and low-speed structures or between both. Mode ϕ^3 is an s-shaped fluctuation in spanwise direction caused by secondary instabilities.[26] The results document the early presence of streamwise disturbances in the transition process. They appear as streak-like patterns in streamwise orientation, in combination with spanwise instabilities, which also start growing very near to the wall.

The measurement area can be enlarged by finer lens arrays that are manufactured lithographically as well as smaller image sections around the micro-pillars. These improvements should allow simultaneous imaging of several hundred micropillars.

V. CONCLUSIONS

The present paper is about a wall shear stress sensor consisting of a combination of channelling optics and flow sensitive hair, called micro-pillars. The two-dimensional mean wall shear stress distributions and its fluctuation are measured.

The self-designed channelling optics consists of a long distance microscope (LDM), lens and aperture array. Compared to imaging with a conventional LDM, the required CCD chip area for covering the same area of sensory hair is reduced by nearly one order of magnitude. Therefore, the presented sensor is superior for high-speed imaging that requires high image magnification.

The magnitude of deflection of a single micro-pillar is a measure for the wall shear stress.[6] Enhanced detection of the fluid-imposed deflections of the micro-pillars enables highest spatiotemporal resolution to date. The dynamic deflection of twenty-one distributed micro-pillars is recorded at 3.000 fps. The measurement uncertainty for the wall shear stress is 7 mPa. The sensor can be used for frequency measurements up to 1.300 Hz without ringing of the micro-pillars. The main benefit of the sensor is to detect flow features, like

vortices, with much less influence on the flow compared to other sensors like micro-fences.[31] The sensor is applied to a wall jet. First results are dominant modes of wall shear stress fluctuations in the transitional region.

In our opinion, the sensor has great potential for tribology and turbulence research in air. Fields of application may be optimization of turbine blades and in-situ control of pipeline or convection flows.

[1]M. El-Desouki, M. Jamal Deen, Q. Fang, L. Liu, F. Tse, and D. Armstrong, Sensors **9**, 430 (2009).

[2]T. Wong and A. K. Agrawal, Meas. Sci. Technol. **17**, 1503 (2006).

[3]S. Brian, *Proceedings of the 15th International Symposium on Applications of Laser Techniques to Fluid Mechanics*, Lisbon, 2010.

[4]S. Thoroddsen, T. Etoh, and K. Takehara, Annu. Rev. Fluid Mech. **40**, 257 (2008).

[5]C. Skupsch, H. Chaves, and C. Brucker, Rev. Sci. Instrum. **82**, 83705 (2011).

[6]C. Brücker, J. Spatz, and W. Schröder, Exp. Fluids **39**, 464 (2005).

[7]C. Brücker, J. Phys.: Condens. Matter **23**, 184120 (2011).

[8]S. Grosse and W. Schröder, J. Fluid Mech. **633**, 147 (2009).

[9]C. Brücker, D. Bauer, and H. Chaves, Exp. Fluids **42**, 737 (2007).

[10]B. E. Launder and W. Rodi, Prog. Aerospace Sci. **19**, 81 (1981).

[11]R. A. Bajura and A. A. Szewczyk, Phys. Fluids **13**, 1653 (1970).

[12]J. G. Eriksson, R. I. Karlsson, and J. Persson, Exp. Fluids **25**, 50 (1998).

[13]A. Dejoan and M. A. Leschziner, Phys. Fluids **17**, 1 (2005).

[14]F. B. Hsiao and S. S. Sheu, Aeronaut. J. **100**, 373 (1996).

[15]M. B. Glauert, J. Fluid Mech. **1**, 625 (1956).

[16]S. Kunze, H. Chaves, and C. Brücker, Exp. Fluids **45**, 573 (2008).

[17]M. T. Tachie, R. B. Balachandar, and D. B. Bergstrom, Exp. Fluids **33**, 351 (2002).

[18]D. Bauer, H. Chaves, and C. Brücker, Meas. Sci. Technol. **20**, 73001 (2009).

[19]D. Douillet, E. Rolley, C. Guthmann, and A. Prevost, Physica B: Condens. Matter **284**, 2059 (2000).

[20]A. E. Conrady, *Applied Optics and Optical Design, Part Two* (Dover, New York, 1992).

[21] J. M. Geary, *Introduction to Lens Design* (Willmann-Bell, 2007).

[22] M. Born and E. Wolf, *Principles of Optics* (Cambridge University Press, Cambridge, England, 2009).

[23] J. Duparré and R. Völkel, Proc. SPIE **6196**, 619607 (2006).

[24] J. Duparré, P. Schreiber, A. Matthes, E. Pshenay-Severin, A. Bräuer, A. Tünnermann, R. Völkel, M. Eisner, and T. Scharf, Opt. Exp. **13**, 889 (2005).

[25] K. Kim, S. Park, J. B. Lee, H. Manohara, Y. Desta, M. Murphy, and C. H. Ahn, Microsyst. Technol. **9**, 5 (2002).

[26] C. H. K. Williamson, Annu. Rev. Fluid. Mech. **28**, 477 (1996).

[27] H. Schlichting and K. Gersten, *Boundary-Layer Theory* 10th ed. (Springer, New York, 2006).

[28] S. Tomotika and T. Aoi, Q. J. Mech. Appl. Math. **IV**, 401–406 (1951).

[29] K. Colella and W. Keith, Exp. Fluids **34**, 253 (2003).

[30] G. Berkooz, P. Holmes, and J. L. Lumley, Annu. Rev. Fluid. Mech. **25**, 539 (1993).

[31] S. Pirskawetz, H.-H. Fernholz, M. Schober, and E. Obermeier, Exp. Fluids **36**, 593 (2004).